





Time-dependent Photoionization Modeling of Warm Absorbers: High-resolution Spectra and Response to Flaring Light Curves

Dev R. Sadaula^{1,2}  and Timothy R. Kallman¹ ¹ NASA Goddard Space Flight Center, 8800 Greenbelt Road, Greenbelt, MD 20771, USA² University of Maryland Baltimore County, 1000 Hilltop Circle, Baltimore, MD 21250, USA

Received 2023 August 1; revised 2023 October 10; accepted 2023 October 18; published 2024 January 8

Abstract

Time-dependent photoionization modeling of warm absorber (WA) outflows in active galactic nuclei can play an important role in understanding the interaction between WAs and the central black hole. The WA may be out of the equilibrium state because of the variable nature of the central continuum. In this paper, with the help of time dependent photoionization modeling, we study how the WA gas properties change with time and how it reacts to changing radiation fields. Incorporating a flaring incident light curve, we investigate the behavior of WAs using a photoionization code that simultaneously and consistently solves the time-dependent equations of level population, heating and cooling, and radiative transfer. We simulate the physical processes in the gas clouds, such as ionization, recombination, heating, cooling, and the transfer of ionizing radiation through the cloud and present high-resolution time-resolved absorption spectra. We demonstrate that time-dependent radiative transfer is important and the calculations that omit this effect quantitatively and systematically underestimate the absorption. Time-dependent photoionization models provide crucial insights into the characteristics of WAs and can be used to constrain their density and spatial distribution.

Unified Astronomy Thesaurus concepts: Astrophysicists (105); Warm ionized medium (1788); X-ray quasars (1821); Time domain astronomy (2109); Quasars (1319)

1. Introduction

Active galactic nuclei (AGNs) are characterized by energetic phenomena, including the emission of radiation across the electromagnetic spectrum, ranging from radio waves to X-rays. This, together with the existence of a supermassive black hole at the center, hints at the existence of gas flows, both inward and outward, near the center. Such gas flows can be studied observationally by observing the absorption and emission produced by them. Many AGNs appear to have an ionized outflows, known as the warm absorbers (WAs), which intercept and absorb specific wavelengths of light, resulting in distinctive absorption features in the observed X-ray spectra. The study of these absorption features provides valuable insights into the physical properties and dynamics of the absorbing gas.

WAs experience temporal fluctuations in the radiation continuum coming from the central regions of AGNs. The brightness of the AGN varies over time owing to flare events such as alterations in the black hole's accretion rate or interactions with its surroundings. A key component of the study of WAs and their evolution is comprehending how they react to these flares.

The effect of continuum variability is most important when the timescales of the intrinsic microscopic processes characterizing the ionization state and temperature are comparable with the variability timescale of the central source. If so, it is important to perform time-dependent calculations. AGN variability has been extensively observed and reveals significant variability ($\geq 20\%$) on timescales as short as $\sim 10^3$ s (Silva et al. 2016). Time-dependent photoionization has been

explored previously in various astrophysical contexts. Examples include the time-dependent cooling in photoionized intergalactic gas (Gnat 2017); time-dependent radiative transfer equation as applied to AGN outflows and gamma-ray bursts (van Adelsberg & Perna 2012); time evolution of H II regions, including the time dependence of radiation transfer (García et al. 2013); and recent models for time-dependent photoionization modeling of AGN outflows by us (Sadaula et al. 2023, hereafter Paper I) and by Rogantini et al. (2022) and Luminari et al. (2023).

Time-dependent photoionization analysis of a gas exposed to a variable source can be used as a density diagnostic. When the illuminating flux varies, the mean ionization state of a gas responds on a timescale dependent on the flux and the gas density. For a gas initially in equilibrium, the flux and density are proportional to each other via the ionization parameter. Gas with low density reacts slowly to variations in the ionizing flux; response to a varying flux will be averaged over a long timescale. When the flux changes for a gas with a high density (e.g., $\geq 10^{10} \text{ cm}^{-3}$ for the cases of interest here), the gas reacts swiftly and largely maintains the equilibrium state. Gas of intermediate gas density reacts to the flux change but with a delay or smearing in time. Based on this delay, it is possible to deduce the density of the gas (Nicastro et al. 1999).

In our previous work (Paper I), we modeled time-dependent ionization of WAs in the idealized situation in which the gas is exposed to a flux that varies with a simple step up from a lower to a higher flux, or a step down from a higher to a lower flux. We also used a relatively crude energy grid and so produced spectra with a resolution appropriate to low-resolution detectors, i.e., resolving power $E/\Delta E \sim 10$. In the present study, we explore the behavior of WA response to gas exposed to flaring light curves. We present the details of the time evolution of the relevant quantities: ion fractions, temperature, and the transmitted spectrum. The transmitted spectra are

calculated using a full XSTAR (Kallman & Bautista 2001) atomic database. The ion fractions obtained from time-dependent photoionization calculations are used to simulate the high-resolution transmission spectra and therefore produce spectra with resolving power $E/\Delta E \sim 1000$. In addition, we examine the effects of modeling the outflow considering the absorber as if it had a single spatial zone. It implies the exclusion of the radiative transfer equation from the set of time-dependent equations. Even though this method is computationally efficient compared to the multizone approach and gives nearly the same results for relatively smaller columns, it departs noticeably for a higher column of absorbers.

In the rest of the paper, we present the model and assumptions in Section 2, the results for the step-up model in Section 3, the result for the flare model with multiple spatial zones in Section 4, and the result for the flare model for a single-zone cloud in Section 5. Then, we present our conclusions in Section 6. The essential equations, assumptions, and numerical methods are presented in the appendices since much of this is a summary of our previous work (Paper I).

2. Models and Assumptions

In Paper I, we studied a range of parameter values affecting WA models: gas densities, ionization parameters, column densities, and continuum variability light curves. Even though many types of models were presented in Paper I, we limited our calculation to relatively low spectral resolution. In addition, all the models were run for a light curve consisting of a single sudden change in the source luminosity, either upward or downward. We term these step-up or step-down models. The results from Paper I give insight into the evolution of the gas in response to a sudden change in the ionizing luminosity and the importance of the time-dependent calculation. However, in order to compare our model calculations with observations, we need to produce a high spectral resolution and consider more realistic light curves for the illuminating flux.

2.1. Ionization Parameter

The ionization parameter is a convenient description of the ionization and temperature of a photoionized gas under the assumption of equilibrium. If so, the ionization parameter can be defined as

$$\xi = \frac{L_{\text{ion}}}{n_{\text{H}}R^2} = \frac{4\pi F_{\text{ion}}}{n_{\text{H}}}, \quad (1)$$

where L_{ion} is the ionizing luminosity of the source, F_{ion} is the ionizing flux, and both of these quantities are integrated from 1 to 1000 Ry. R is the distance of gas from the ionizing source. This definition was first introduced by Tarter et al. (1969). The other way of defining the ionization parameter is $U = \int_{\epsilon_1}^{\epsilon_2} L_{\epsilon} / (\epsilon 4\pi R^2 n_{\text{H}} c) d\epsilon$, where L_{ϵ} is the ionizing luminosity per energy interval and c is the speed of light. U and ξ are easily convertible to each other for a given spectral energy distribution (SED) of the ionizing continuum. For the spectrum shape we adopt here, i.e., a single power law from 1 to 1000 Ry with energy index -1 , the conversion is $U = \xi/56.64 \text{ erg cm s}^{-1}$. The higher the ionization parameter, the more ionized the gas and vice versa. WA components generally exist either in the low ionization state of $\xi \sim 1 \text{ erg cm s}^{-1}$ or in

the high ionization state of $\xi \sim 100 \text{ erg cm s}^{-1}$ (Laha et al. 2014).

It is important to clarify the usage of luminosity and flux. These two quantities are interconnected through Equation (1). Luminosity refers to the total ionizing luminosity emitted by the source, while flux represents the luminosity of the source divided by the area of the sphere at the specific point of interest within the cloud. The flux is a convenient description of the radiation strength and its effects on gas locally, while luminosity is a useful measure of the global energetics of the central source.

2.2. Models

The free parameters in our models include hydrogen number density (n_{H} ; hereafter hydrogen gas density unless otherwise stated), hydrogen column density (N_{H} ; hereafter column density means hydrogen column density unless otherwise stated), ionization parameter (ξ), the shape of the incident radiation as described by the SED, and element abundances. We have created models for WA outflows depending mainly on the type of incident light curve. These are (1) a step-up model, (2) a flare model with multiple-zone consideration, and (3) a flare model with single-zone consideration. We refer to the step-up model as model 1, a flare model with multiple-zone consideration as model 2, and a flare model with single-zone consideration as model 3 in the subsequent sections for simplicity. The details of these models are described in the corresponding sections.

2.3. Assumptions

Since this work is an early step toward exploring photoionized plasma in nonequilibrium conditions, we attempt to make our results general and illustrate the general behavior of time dependence. Therefore, we have made several key approximations:

1. We approximate the gas to be static, with no expansion of the gas and no velocity gradient. For a supersonic flow, such as in a WA, the bulk forces, whatever they are, dominate over internal dynamics in the cloud (Proga et al. 2022). If so, our models can be applied by adding a blueshift. We acknowledge that this effect can be important, but it is not included in the results presented here. We can calculate models that can be refined for specific situations, and we plan to do so in future work.
2. We assume that the outflowing gas has constant density throughout. This assumption is partially justified by the physical thickness of the cloud, which is less than 10% with respect to the distance from the ionizing source, as shown in Paper I. If so, the imprint of any large-scale spherical flow will be small. However, we acknowledge that there may be a density gradient in the case of WAs associated with dynamical effects such as ram pressure, which will be considered in future work.
3. We have not included emission in our radiative transfer calculation. This approximation is justified if the covering fraction of the absorber relative to the central source is small; this appears to be the case for most observed WAs. For most observed WA spectra, emission features are weak or absent (Kaspi et al. 2001; Kaastra et al. 2002). However, including emissions is on our list of tasks for

future work since the emission is likely to be important in other time-dependent applications.

2.4. High-resolution Spectra

Time-dependent calculations require the simultaneous solution of the equations describing the ionic level populations, temperature, and radiation field for all level populations, spatial zones, and photon energies. This corresponds to a very large number of simultaneous ordinary differential equations; the standard XSTAR database has $\sim 3 \times 10^4$ energy levels. Running these full schemes is extraordinarily time-consuming and sometimes gives unstable solutions if the number of equations is too large. This necessitates a simplification of this system of equations to make it tractable. That is, we simplify the energy level structure of the ions in the gas. To do this, we have created an atomic database that describes each ion using three levels: the ground level, one excited bound level, and the continuum (ionized) level. For the one bound excited level, we adopt an ad hoc description: the level energy is $0.8 \times E_{\text{th}}$, where E_{th} is the ionization potential of the ion. We include electron impact collisional excitation to the level for the ions H^0 , He^0 , and He^+ with an effective collision strength (upsilon) with a value of 1.4–2.7 depending on temperature. The excited level is a pseudolevel, and the energy of that level is chosen in such a way that the temperature versus ionization parameter (ξ) curve can agree as closely as possible with the temperature versus ionization parameter (ξ) curve obtained from the full XSTAR databases. This is illustrated in Figure 2 of Paper I. We include all of the ions that are in XSTAR in the newly created database, though the simulations in this paper include only a subset of them. Paper I gives more details about this small database.

In addition, we are limited by the number of time, position, and energy grid points that can be included in our computation while solving the discretized time-dependent equation of level population, energy balance, and radiative transfer. The energy grid we can use for such calculations is inadequate for calculating high-resolution spectra. To address this, we created a two-step technique:

1. We first run the time-dependent photoionization code with reasonable energy, position, and energy grid numbers using the small subset of the XSTAR database, with each ion represented by two bound levels plus a continuum.
2. The ground-level populations, which are mainly responsible for the absorption of the ionizing radiation of the source, are then used to produce high-resolution spectra using the spectral fitting model package WARMABS.³ WARMABS uses the full XSTAR database and can handle arbitrary energy grid spacing. We then use the opacities from WARMABS to calculate the emergent absorption spectrum via the formal solution to the radiative transfer equation (including the time delays associated with light-travel time).

3. Results: Model 1, Step-up Model

Paper I comprehensively discussed the general behavior of time-dependent photoionized models. It covered various

aspects such as ion fractions, temperature, and transmitted spectra. The current study expands on our previous work by incorporating a high-resolution spectrum. We have done this using the full XSTAR database and adding a more dense energy grid. We also track the evolution of the gas until it returns to a state of high flux equilibrium. Model 1 illustrates the progressive changes observed in the high-resolution spectra when exposed to a step-up flare incident light curve.

As was true for our models in Paper I, we capture the time dependence of the propagation of the radiation through the cloud by solving the time-dependent radiation transfer equation. We employ a multiple-zone approach by dividing the gas cloud into distinct slices and solving the radiative transfer equation (Equation (A5) presented in Appendix A) on this grid using a finite-difference representation.

3.1. Model Parameters

Model 1 has the following input parameters: gas density 10^7 cm^{-3} ; column density $9.0 \times 10^{22} \text{ cm}^{-2}$; initial ionization parameter (ξ_1) $\sim 50 \text{ erg cm s}^{-1}$; incident ionizing spectral shape of a power law with energy index -1 ; initial luminosity of the source $10^{44} \text{ erg s}^{-1}$; and it includes the elements H, He, C, O, Si, and Fe. The incident ionizing radiation flux suddenly increases by a factor of 3 at the beginning of the simulation.

3.2. Step-up Light Curve

In Figure 1, we present the input light curve for model 1. The initial luminosity of the source is set at $10^{44} \text{ erg s}^{-1}$, and it is subsequently increased to $3.0 \times 10^{44} \text{ erg s}^{-1}$ at $\sim 20 \text{ s}$. We have included five vertically dotted green lines to highlight specific times for which we will display the spectra. These times are chosen such that the changed radiation field has completely emerged through the cloud. The simulation for this model is conducted for 10^8 s .

3.3. Absorption Spectra

Figure 2 displays the evolution of transmitted spectra for model 1. Each panel illustrates the transmitted spectrum at a specific moment in time. It is important to note that the time it takes for the radiation to propagate from the source to the illuminated face of the absorber is not considered. The simulation begins with the arrival of the changed flux at the face of the cloud. The initial spectrum showcases the absorption features and characteristics before the increase in luminosity occurs. Over time, as the higher flux propagates through the absorber, the transmitted spectra in subsequent panels exhibit changes in the absorption features. These changes are a consequence of the altered ionization and excitation within the gas due to the increased luminosity of the ionizing source. The simulation is primarily on the effects of the sudden change in luminosity once it reaches the surface of the cloud, the illuminated face. Figure 2 visually represents the evolving transmitted spectra and their response to the abrupt increase in ionizing source luminosity. It provides information about the time-dependent behavior of the absorber and the impact of changes in the incident flux on its observed spectral features.

The spectra presented in Figure 2 constitute many absorption features. The absorption features spanning the energy range $\simeq 0.2\text{--}0.7 \text{ keV}$ primarily arise from the absorption of carbon (C V and C VI), silicon, and iron L-shell ions. The second group

³ <https://heasarc.gsfc.nasa.gov/docs/software/xstar/xstar.html>

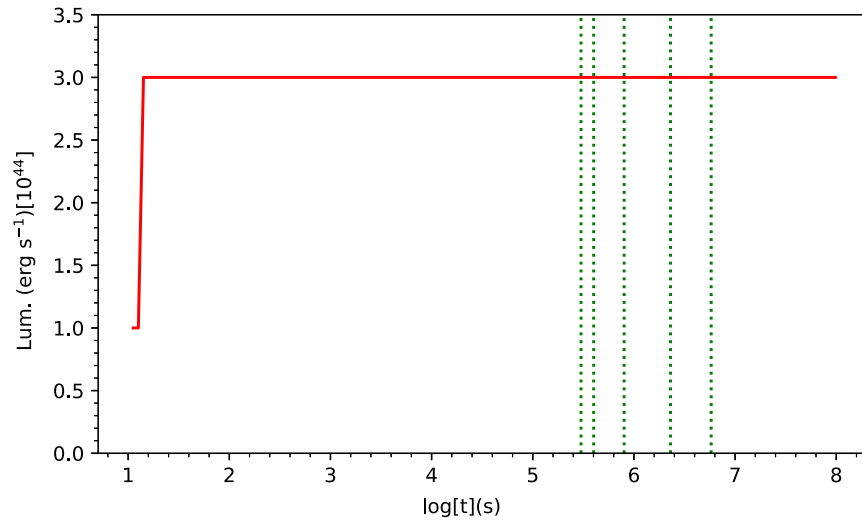


Figure 1. The light curve at the face of the cloud (red line) in units corresponding to source luminosity. The source luminosity was changed by a factor of 3 to a higher value (3.0×10^{44} erg s $^{-1}$). The five vertical green dotted lines are times at a high flux state. We have chosen them to illustrate the evolution of the model absorption spectrum.

of absorption features, located at $\simeq 0.75$ keV, predominantly results from iron ions. The absorption edge at $\simeq 1$ keV is primarily influenced by iron and oxygen. The interaction between these ions and incident radiation gives rise to the distinctive absorption edge observed in this energy range. Throughout the spectrum, absorption lines arise from a wide range of ions associated with various elements. In each panel, three different spectra are presented: the red curve represents the high flux equilibrium spectrum, the orange spectrum corresponds to the low flux equilibrium spectrum, and the blue curve represents the time-dependent spectrum. The green curves are obtained by multiplying the low flux equilibrium spectrum by three. These reference spectra help to visualize how the ionized absorber changes its opacity over time owing to the sudden change in the luminosity of the source from low to high. These spectra allow for a comparative analysis of the evolving absorption features and their variations in response to changing flux conditions. By examining the figure and the different spectra presented, it is possible to gain a deeper understanding of the time-dependent behavior of the absorption features, as well as the contributions of different ions and elements to the overall spectrum.

The first panel of Figure 2 corresponds to the case before the changed radiation field arrives at the back of the cloud. The time it takes light to cross this cloud for this model is $\simeq 3 \times 10^5$ s. This is why the orange and blue spectra overlap until this time. When the altered radiation arrives at the back of the cloud, the blue spectrum changes toward the red spectrum and overlaps with the green spectrum because the gas has not yet had a chance to change its ionization state, as seen in the second panel. Since the opacity of the gas cloud decreases over time owing to a high ionizing radiation field, the gas becomes more transparent, and the spectrum starts to move closer to the red curve and farther from the green curves. This model takes $\sim 5.8 \times 10^6$ s for the gas to reach an equilibrium state corresponding to the high flux. This is the time including the effect of photoionization and thermal equilibrium. The time-scale of thermal equilibrium is much longer than the photoionization equilibrium (Paper I).

We have generated a ratio plot, depicted in Figure 3, to illustrate the dynamic evolution of absorber opacity. To achieve

this, we created two distinct ratios against energy at various time points. The blue curves represent the ratios of spectra resulting from time-dependent photoionization equilibrium calculations (blue spectra in Figure 2) to those of the high flux equilibrium spectra (red spectra in Figure 2). On the other hand, the green curves denote the ratios of three times the low flux equilibrium spectrum (green spectra in Figure 2) to the ultimate high flux equilibrium spectra.

The green line within Figure 3 serves as a reference line for comparing alterations in transmitted absorption spectra at various times during the simulation. The blue curve in the first panel corresponds to the time before the altered radiation field reached the back of the cloud. This is why the blue and green curves differ in absorption features and continuum. In the second panel, both of these curves overlap each other. The altered radiation field has just arrived at the back of the cloud by this time. In the rest of the panel, the green curve starts to depart at absorption features because the gas starts to be ionized and becomes transparent as time passes. The opacity of the gas changes until the blue line becomes nearly horizontal, and the ratio becomes 1. This corresponds to the final flux ionization state of the gas.

4. Results: Model 2, Flare Model with Multiple Zones

In this section, we investigate the response of the gas cloud to a flare-like event, aiming to simulate scenarios observed in certain variable AGNs where a sudden increase in luminosity occurs, followed by a return to the initial state. This behavior may be attributed to a rise in accretion rate onto the central black hole. As was the case with model 1, to capture this phenomenon, we employ a multiple-zone approach by dividing the gas cloud into distinct slices and incorporating the radiative transfer equation into our model.

By considering the radiative transfer equation, we account for the interaction of radiation with the gas in each zone. This allows us to examine how the radiation propagates through the cloud and affects its physical and ionization properties. The multiple-zone approach provides a more comprehensive and detailed description of the gas cloud's response to the flare, enabling us to capture the spatial variations and dynamic

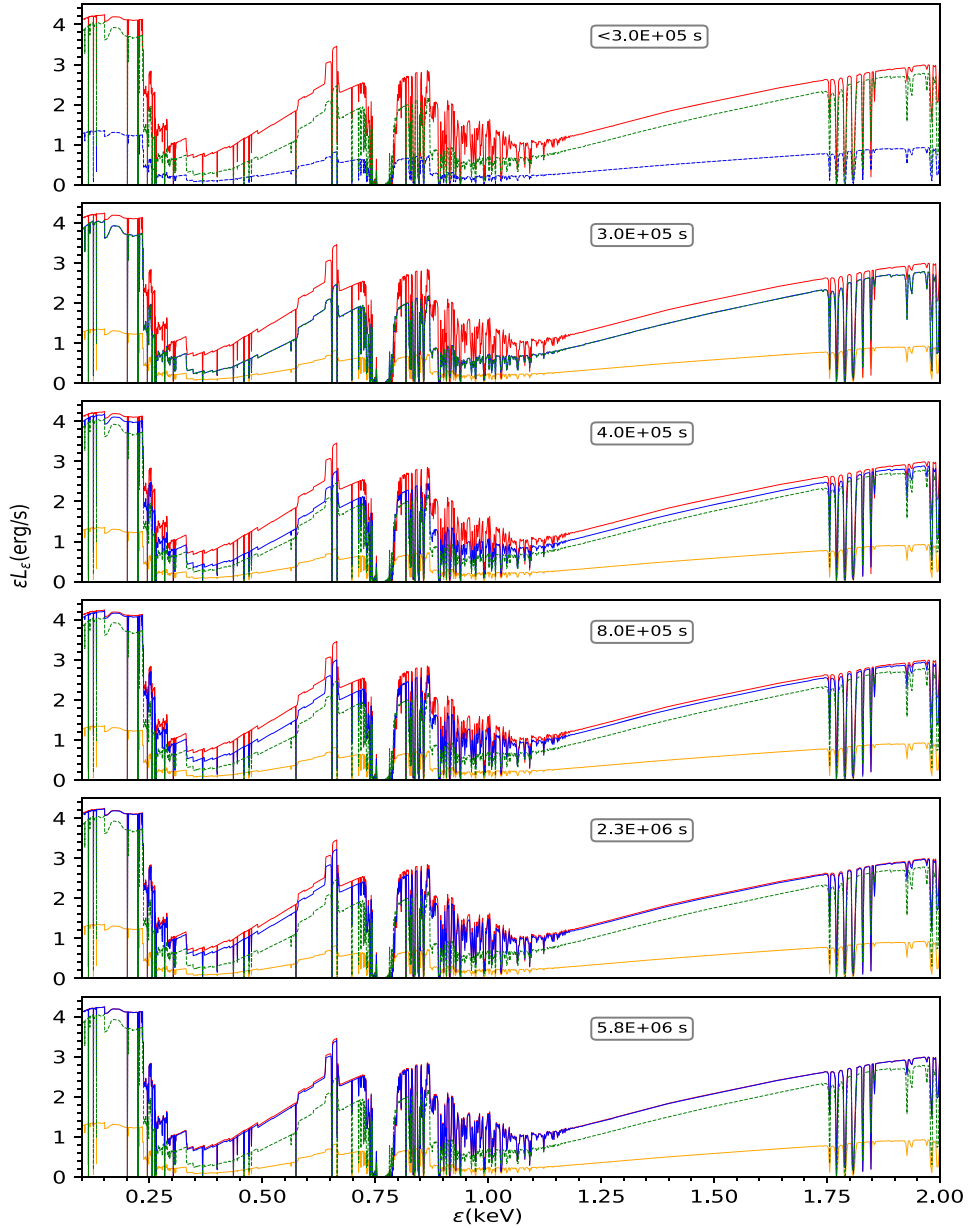


Figure 2. Snapshot of the evolution of absorption spectra for a step-up model with gas density $n = 10^7 \text{ cm}^{-3}$. The y-axes represent the transmitted luminosities (ϵL_ϵ), and the x-axes represent the photon energies (ϵ). The units of ϵL_ϵ are $10^{43} \text{ erg s}^{-1}$. The orange curves represent lower flux equilibrium spectra, the red curves show the high flux equilibrium spectra, and the blue curves show the evolution of transmitted spectra during the simulation. We have also plotted the green spectra for reference, obtained by multiplying a low flux equilibrium spectrum by a factor of 3. The times in the box correspond to the vertical dashed green lines on the light curve in Figure 1.

processes occurring within the cloud. This enables us to study the evolution of absorption features, emission lines, and other spectral characteristics as the flare propagates through the cloud.

The inclusion of radiative transfer in our model allows us to account for the time delays associated with the propagation of radiation through the cloud. As the flare radiation travels through the different zones, it interacts with the gas, leading to ionization changes and the emergence of absorption and emission features at different stages of the flare evolution.

By analyzing the time-dependent spectra obtained from the multiple-zone approach, we can explore the evolution of the absorption features and the corresponding ionization states of various elements in the cloud. This enables us to investigate the interplay between the radiation field, ionization processes, and the physical conditions within the cloud during the flare event.

In the following sections, we present the detailed results of our multiple-zone modeling approach, including the time-dependent evolution of the spectra, the variation of absorption features, and the ionization states of different elements across the cloud. These results provide insight into the behavior of WAs in response to flaring events, shedding light on the underlying physical processes in AGNs and their impact on the observed spectra.

4.1. Model Parameters

Model 2 has gas density of 10^7 cm^{-3} , initial luminosity of the source of $10^{44} \text{ erg s}^{-1}$, initial ionization parameter (ξ_1) of $\sim 81 \text{ erg cm s}^{-1}$, column density of 10^{22} cm^{-2} , and the incident ionizing spectral shape of the power law with energy index -1 , and it includes elements H, He, C, N, O, Ne, Mg, Si, S, and Fe.

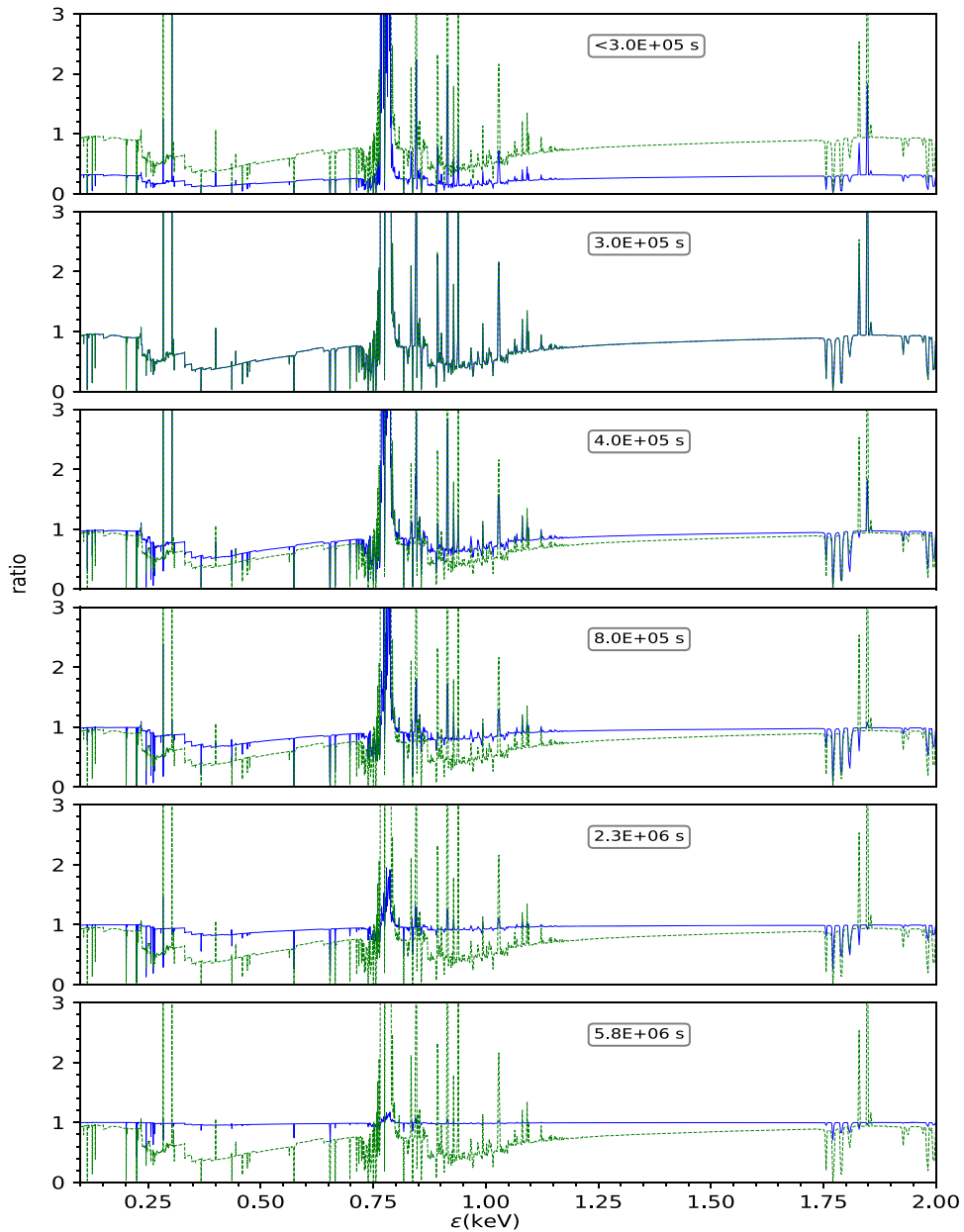


Figure 3. Snapshot of the absorption spectra evolution by plotting the spectral ratio for model 1. The blue line is the ratio of time-dependent spectra to the final high flux equilibrium spectra, while the green line is the ratio of three times the low flux equilibrium spectra to final high flux equilibrium spectra (this is plotted for reference). The times in the box correspond to the vertical dashed green lines marked on the light curve in Figure 1. The details are given in the description.

The incident ionizing radiation flux suddenly increases by a factor of 10. The cloud in this model is divided into 60 spatial zones. The simulation is run for 10^5 s.

4.2. Flare Light Curves

Our study considers the incident light curve, as depicted in Figure 4. The red curve represents the incident light curve at the illuminated face of the cloud, whereas the green curve is at the back of the cloud. This incident light curve exhibits three distinct regions, each with its own characteristics. The first region corresponds to a linear increase in source luminosity until 10^4 s. During this phase, the flare is in its initial rising state, gradually increasing in intensity. The second region of the light curve represents a high luminosity state that remains constant for an additional 10^4 s. This phase corresponds to the

peak of the flare, where the source maintains a steady high luminosity. After the high state, the third region shows a linear decrease in flux over a duration of 10^4 s. This marks the declining phase of the flare, where the luminosity gradually decreases with time until it reaches a low luminosity state. Overall, the entire variability time of the flare is 3×10^4 s, which encompasses the rising, peak, and declining phases.

In our multiple-zone modeling approach, we consider the propagation of the flare through the gas cloud. As the flare progresses deeper into the cloud, its temporal behavior changes, resulting in a smoother variation compared to the initial light curve. This effect can be observed by examining the green line in Figure 4, which represents the light curve obtained at the back of the cloud.

The time for the flare to travel through the cloud is determined by the sum of three components: the variability

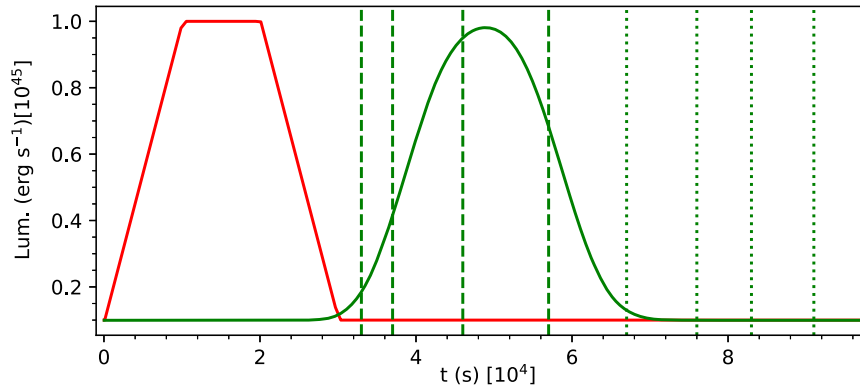


Figure 4. The light curves at the face (red curve) and at the back of the cloud (green curve) for model 2. The source luminosity changed by a factor of 10. The variability time of the flare is 3.0×10^4 s. The first four vertical green dashed lines are at different times during the flare, and the last four green dotted lines are at a time when the luminosity settles at a low state.

Table 1
The Photoionization and Recombination Times for Some Important Ions Contributing to the Absorptions

Ions	C VI	O VII	O VIII	Si XIII	Si XIV	Fe XV	Fe XVI
Photoionization time (s)	1.7×10^3	3.1×10^3	1.0×10^0	1.2×10^2	3.7×10^2	2.7×10^1	2.6×10^1
Recombination time (s)	2.0×10^4	1.4×10^4	2.1×10^4	5.0×10^3	2.0×10^3	3.3×10^2	2.2×10^2

Note. This is at the face of the cloud and calculated using equilibrium approximation at a low flux state.

time of 3×10^4 s, the light-travel time, and the propagation time. The light-travel time is the time it takes for the flare to travel from the front of the cloud to the back in the absence of any absorption. In our model, the light-travel time is estimated to be $\sim 3.3 \times 10^4$ s. Therefore, the total time for the flare to traverse through the entire cloud is $\sim 7.0 \times 10^4$ s, as shown in Figure 4. The propagation time primarily comes from the variable absorption process of ionizing radiation within the cloud. It depends on the ratio between the number of atomic species undergoing ionization within a specific spherical shell and the rate of ionizing photons emitted by the source in case of increasing source luminosity. The propagation time, therefore, depends on the ionization and recombination time of the ions. For a more comprehensive and quantitative description of the propagation time, please refer to Paper I. For reference, the photoionization and recombination times of some important ions are presented in Table 1. These times are calculated at the illuminated face of the cloud, using equilibrium calculation for the low luminosity value of the source. These times are taken from the simulation and hence include some errors. Most of the error appears as a result of the coarse energy grids and the simplified database we have used.

4.3. Level Populations

This study examines the response of a gas cloud to changes in the radiation field. It is important to note that this response is not instantaneous and simultaneous throughout the cloud. Instead, there is a time delay in the response of the gas at different locations within the cloud. This delay is primarily influenced by the time it takes for the radiation to propagate through the cloud and the absorption processes that occur.

To illustrate this, Figure 5 presents the ion fraction profile of oxygen (O VIII) at different times during the cloud's evolution. The ion fraction profile represents the relative abundance of O VIII ions within the cloud at various spatial locations. The value of the O VIII ion fraction is $\simeq 0.13$ in our simulation. This

differs from the value at this same ionization parameter from Kallman & McCray (1982), which was $\simeq 0.5$. The ion abundance curve for O VIII is shifted when these two calculations are compared. The ion fraction versus ξ curves peaks at $\xi \simeq 15 \text{ erg cm s}^{-1}$ for the calculations shown here, while it peaks at $\xi \simeq 50 \text{ erg cm s}^{-1}$ for the 1982 calculations. For the standard XSTAR code plus database, the peak occurs at $\xi \simeq 25 \text{ erg cm s}^{-1}$. Reasons for these differences include differing energy grids, the simplified version of the atomic database used in our current simulations, and other numerical factors.

At the initial time, when the radiation field starts to impact the cloud, the ion fraction profile of O VIII exhibits its initial distribution. As time progresses, the radiation field propagates through the cloud, reaching deeper into its interior. This leads to changes in the ionization state of the gas.

As depicted in Figure 5, the ion fraction profile of O VIII at later times shows variations compared to the initial profile. The changes in the ion fraction occur gradually as the radiation field penetrates further into the cloud, resulting in a modified ionization state of oxygen. The time is shown in the box for each panel. The first left panel corresponds to the initial flux equilibrium ion fraction profile in the gas. This is before the gas gets flares. In the successive panels of the left column, the ion fractions are shown for increasing time. When the gas receives the flare, the ion fraction starts to change at the face of the cloud first. The ion fraction at the face of the cloud started to change at $\sim 3 \times 10^3$ s, gradually went down as the flare went up, and reached a minimum at $\sim 2.1 \times 10^4$ s (the last panel of the left column) and started to increase as the flare decreased and reached the initial value again at time $\sim 3.9 \times 10^4$ s (sixth panel of the right column).

Propagation of the flare caused the ion fraction to decrease, reach the minimum, remain at a minimum for some time, and increase until it acquired the final low flux equilibrium value at all points in the cloud. The equilibration time at the back of the cloud is the sum of light-travel ($\sim 3.3 \times 10^4$ s), flare

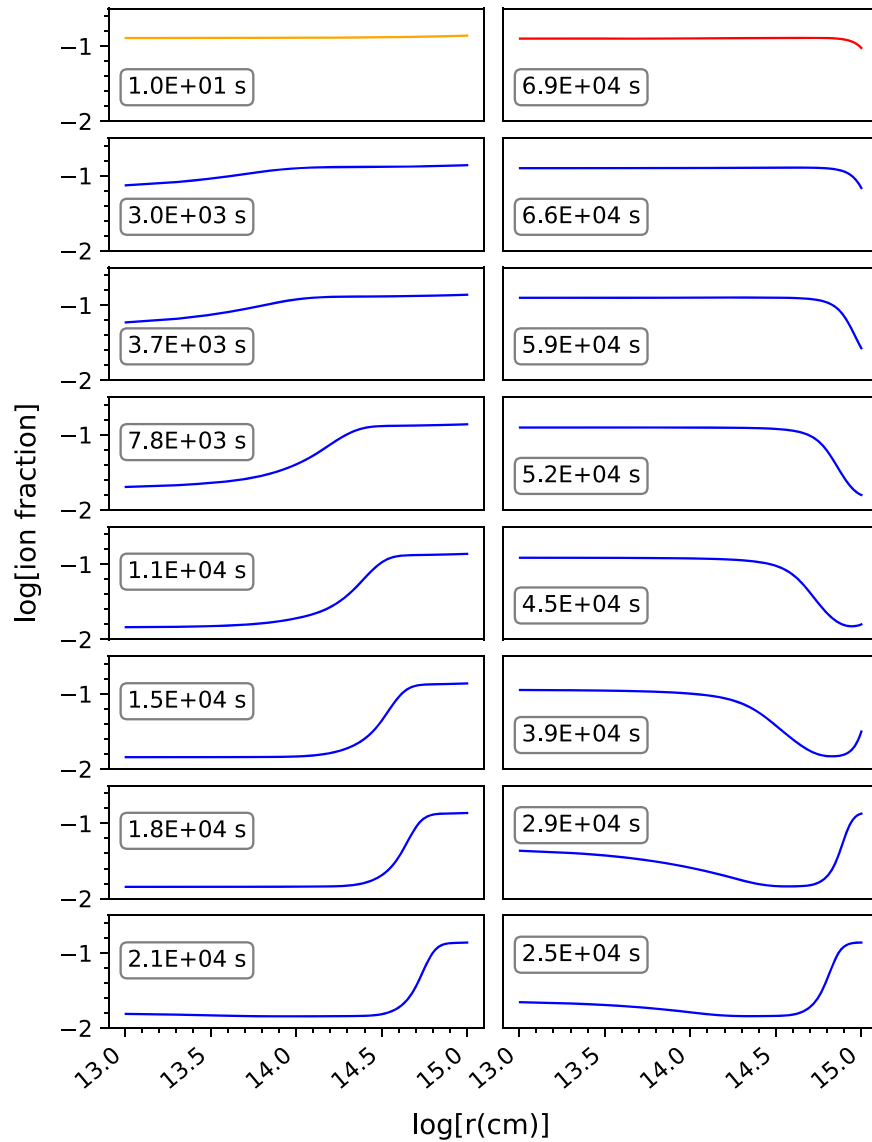


Figure 5. Evolution of O VIII ion fraction profiles for model 2. The x -axis represents the depth r in the gas from the illuminated face, and the y -axis represents the ion fractions. The orange curve represents the initial lower flux equilibrium, while the red curve represents the final low flux equilibrium. Each blue curve corresponds to the quantity at an intermediate time during evolution.

($\sim 3.0 \times 10^4$ s), and response time ($\sim 6.0 \times 10^3$ s), which comes to be $\sim 6.9 \times 10^4$ s (the first panel of the right column). Therefore, it took $\sim 6.9 \times 10^4$ s for the whole gas to return to equilibrium. We note that the times in the panels are increasing going down in the first column and increasing going up in the second column.

The time evolution of the different ions at different spatial points in the cloud can be seen in Figure 6. Each panel corresponds to a different ion except the first (top left) panel. The top left panel shows the temperature evolution in the cloud at different locations. The time-dependent calculation predicts a temperature that evolved very little during the simulation. The temperature changed only by $\sim 10^4$ K for a flare, which increased in flux by a factor of 10. This temperature change is small compared to the change found if the gas were in equilibrium at the corresponding flux. The temperature changes by an order of magnitude in equilibrium approximation because the ionizing luminosity also changes by the same amount. The small increase in temperature in the time-dependent calculation is attributed to

the longer thermal timescale of low-density plasma. The ionizing source stays at a high luminosity state for 10^4 s. This is much shorter than when it takes plasma to be thermalized. The thermal timescale of the plasma is about $\sim 10^5$ s for this model (Paper I). In the rest of the panels, we have shown the evolution of representative ions such as C VI, O VII, O VIII, Si XII, Si XIV, Fe XV, and Fe XVI. The blue curves come from the time-dependent calculation, whereas the orange lines come from the equilibrium approximation. The line that evolves earlier corresponds to the ion fraction at the illuminated face of the cloud, and the one that evolves slowest is at the back of the cloud; the rest are inside the cloud. In this plot, we have shown ion fractions at seven different points in the cloud, including the illuminated face and back of the cloud. The inner spatial points are at $\sim 1.7 \times 10^{14}$ cm, $\sim 3.4 \times 10^{14}$ cm, $\sim 5.0 \times 10^{14}$ cm, $\sim 6.8 \times 10^{14}$ cm, and $\sim 8.5 \times 10^{14}$ cm from the illuminated face. Note that the physical size of the cloud for this model is 10^{15} cm.

For this model, C VI, O VII, and O VIII ions come to the final low flux equilibrium ion fraction value relatively quickly

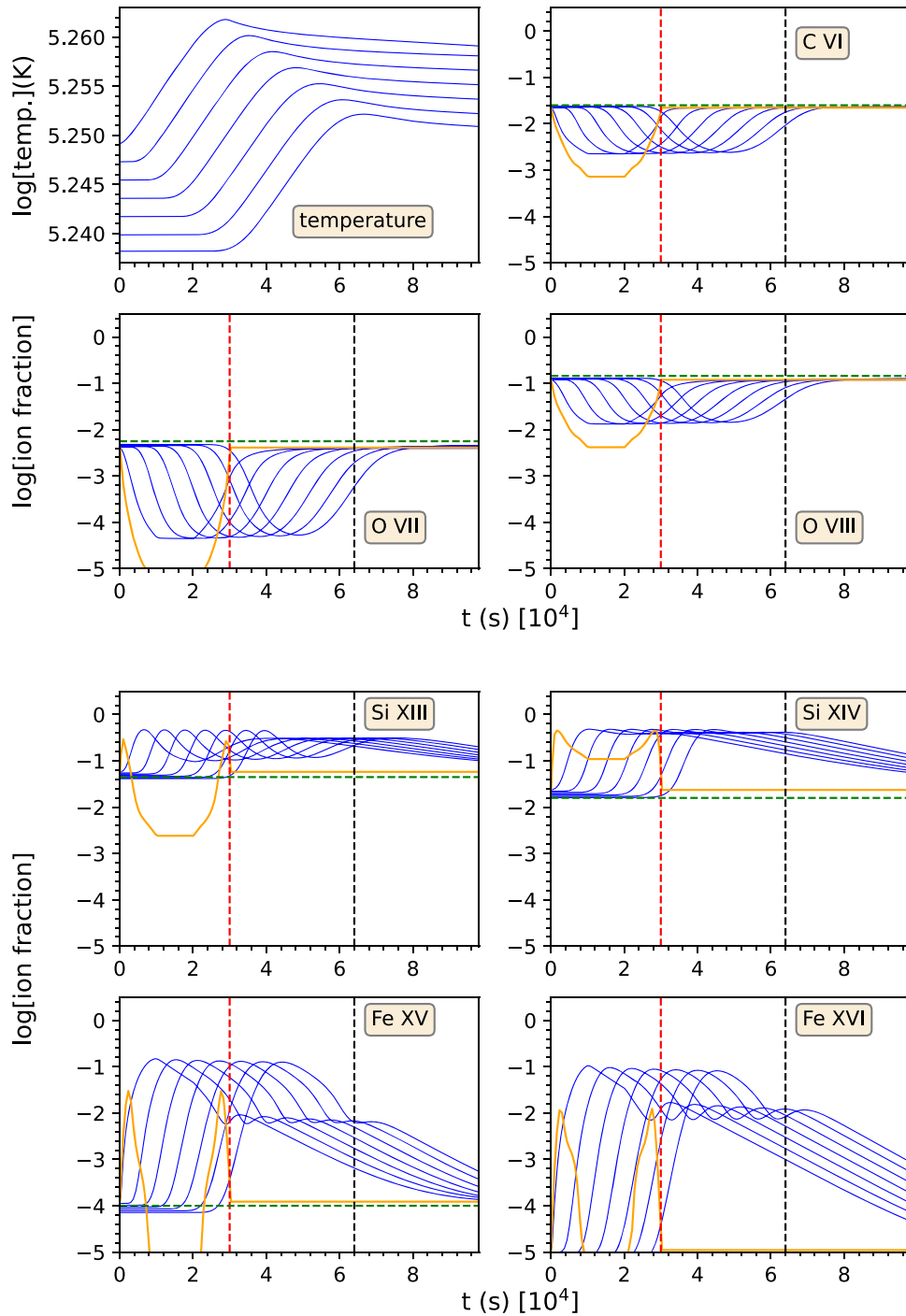


Figure 6. Time evolution of temperature (top left panel) and ion fractions (remaining panels) for model 2. The x -axes are times in units of 10^4 s. Each blue curve in all panels corresponds to a particular spatial point in the cloud. The one that evolves early is at the illuminated face of the cloud, and the latest is at the back of the cloud. The orange curves represent the equilibrium ion fraction at the illuminated face of the cloud plotted for comparison. The horizontal green line represents the equilibrium ion fraction for a low flux state. The red vertical dashed lines represent the time of flare at the face. The black vertical dashed lines, on the other hand, represent the time that it takes to propagate through the cloud completely.

compared to the other ions, such as Si XII, Si XIV, Fe XV, and Fe XVI. The time it takes for an ion to come to equilibrium corresponds to the time it takes the absorption spectrum to come to equilibrium at the relevant energies. The spectral evolution will be discussed in more detail in Section 4.4.

The red dashed vertical line in all the panels indicates the time of the flare, which is 3×10^4 s as seen in the light curve. The black dashed vertical line represents the time it takes for the flare to emerge completely from the cloud. This time is the

sum of the flare time (3×10^4 s) plus the light-travel time ($\sim 3.3 \times 10^4$ s) of the cloud. The green dashed horizontal line is the low flux equilibrium value. All the panels show that, even if the flare has already passed, the ion fraction is still changing. However, the timescale to come to equilibrium is different for different ions. Ions such as C VI, O VII, O VIII, and Fe XV come to the equilibrium value by the time the simulation ends. However, ions such as Si XIII, Si XIV, and Fe XVI do not come all the way to the equilibrium values by the end of the

simulation. They are close to the equilibrium when the simulation is ended; we estimate that it would take an additional $\sim 5 \times 10^4$ s to reach equilibrium for all these ions.

It is important to note that the equilibrium ion fraction values are different from those from the time-dependent calculation. Ions such as C VI, O VII, and O VIII have the same equilibrium ion fraction pattern as they do for time-dependent models. They differ only in magnitude by some fraction. However, for ions such as Si XIII, Si XIV, Fe XV, and Fe XVI, the equilibrium ion fraction is qualitatively different from those from a time-dependent calculation. The equilibrium ion fraction curves have an ‘‘M shape’’ structure owing to the flare. That is, at low flux early in the flare and late in the flare, the ion fractions increase with increasing flux and decrease with decreasing flux. In the middle of the flare, the ion fractions decrease with increasing flux and increase with decreasing flux as the parent element is ionized to higher ion stages. This behavior makes the time-dependent modeling qualitatively different from equilibrium calculations.

The most significant feature of the behavior of some ion fractions versus time is asymmetry. There is a tail-like structure in ions such as Si XIII, Si XIV, Fe XV, and Fe XVI. This implies that when the flux is in the increasing phase of the flare, the ion fraction values change more rapidly than when the flare is in the declining phase. It is important to keep in mind that the time-dependent ion fraction value at any time during evolution does depend on the condition at the previous times together with input parameters such as ionization parameter, time of the flare, density, etc. Once the gas experiences the flare, and if the variability time of the flare is comparable to the photoionization and/or recombination timescale, a delay in the response occurs. This is just because the gas did not have enough time to respond to the change in the radiation field. The reason behind this is the behavior of the dominant microscopic timescale behind the increasing and declining phases of the flare. During the increasing phase, the gas starts to change its ionization state to a higher value, which is determined by photoionization, whereas recombination time plays a dominant role during the declining phase of the flare. Furthermore, the recombination is dominated by dielectronic recombination for these ions, and this process is very temperature sensitive. As shown in Paper I, the temperature is determined by the thermal timescale, i.e., the cooling time, and for this model the cooling time is longer than the recombination time. Thus, the gas remains stuck at a higher temperature late into the simulation, and at this temperature the dielectronic recombination rate is less than it was at the initial equilibrium. This results in the asymmetric ion fraction versus time distribution for these ions. Successive ionization and recombination of the ions with the delayed response result in the complicated shape of ion evolution for these ions.

4.4. Absorption Spectra

Figure 7 showcases the individual elemental contributions to the absorption spectrum. The model includes several elements such as H, He, C, N, O, Ne, Mg, Si, S, and Fe to simulate the response of a cloud to a flaring incident light curve. The figure highlights the relative importance of each element in contributing to the overall absorption spectrum. Among the elements considered, O (oxygen), Si (silicon), S (sulfur), and Fe (iron) dominate the absorption features in the spectrum. While the focus is on these key elements, it is important to note that the full spectrum encompasses absorption lines from all the

included elements. The absorption features arise from a combination of edges and lines associated with the various ions. The energy range shown in the figure is up to 2 keV, as most ions primarily absorb radiation in the soft X-ray band. This range allows for a comprehensive representation of the absorption features resulting from the elemental contributions. The final model spectrum has three deep continuum absorption features at ~ 0.3 , ~ 0.75 , and ~ 1 keV. These are denoted by first, second, and third absorption features in the spectrum described in the following section. In subsequent sections, the figure will be further explored to elucidate the specific absorption features, including edges and lines, present in the spectrum. This analysis will provide valuable insights into the ionization states, physical properties, and dynamics of the gas cloud under investigation.

Figure 8 illustrates the temporal evolution of a modeled observed spectrum in response to a flare-like variation in the ionizing source. The figure consists of eight panels, each representing a specific time interval and displaying the corresponding absorption spectrum. The panels are divided into two sets of four. The first four panels depict the absorption spectrum during the passage of the flare through the cloud, while the last four panels represent the absorption spectrum after the flare has passed. The orange curve in each panel corresponds to an equilibrium spectrum generated using the instantaneous flux. This spectrum represents the expected absorption features without any temporal variations. The blue curves in the figure represent time-dependent photoionization spectra at different points in time during the evolution. These spectra showcase the changes in the absorption features as the flux varies over time at the face of the cloud. By observing the figure, one can see how the absorption spectrum evolves over time in response to the changing flux from the ionizing source. The differences between the yellow and blue curves highlight the impact of temporal variations on the absorption features of the spectrum.

Figure 8 comprises multiple panels, each representing a specific time corresponding to different vertical lines in the associated light curve. In the first panel, the time corresponds to the period before the flare reaches the back of the cloud. At this point, both the equilibrium and time-dependent spectrum overlap significantly. The absence of significant divergence indicates that the spectra are similar, as the increased flux from the flare has not yet reached the cloud’s back. This time interval aligns with the first vertical line in the light curve.

The second panel corresponds to a time of $\sim 3.7 \times 10^4$ s (the sum of the light-crossing time plus the time it took for the flare to reach this luminosity level); the luminosity of the source reaches $\sim 4 \times 10^{44}$ erg s $^{-1}$. In this state, the equilibrium spectrum and the time-dependent spectrum begin to diverge. The equilibrium spectrum exhibits relatively less absorption compared to the time-dependent spectrum. The first and third absorption features, observed in the time-dependent spectrum, are nearly absent in the equilibrium spectrum. This difference arises from the higher ionization level of the gas due to the increased flux value.

The third panel represents the high luminosity state with source luminosity $\sim 10^{45}$ erg s $^{-1}$, crucially showcasing the absence of absorption features in the equilibrium spectrum. In this state, the equilibrium spectrum shows minimal absorption, with most features being eliminated, except for a few weak absorption lines. In contrast, the time-dependent spectrum

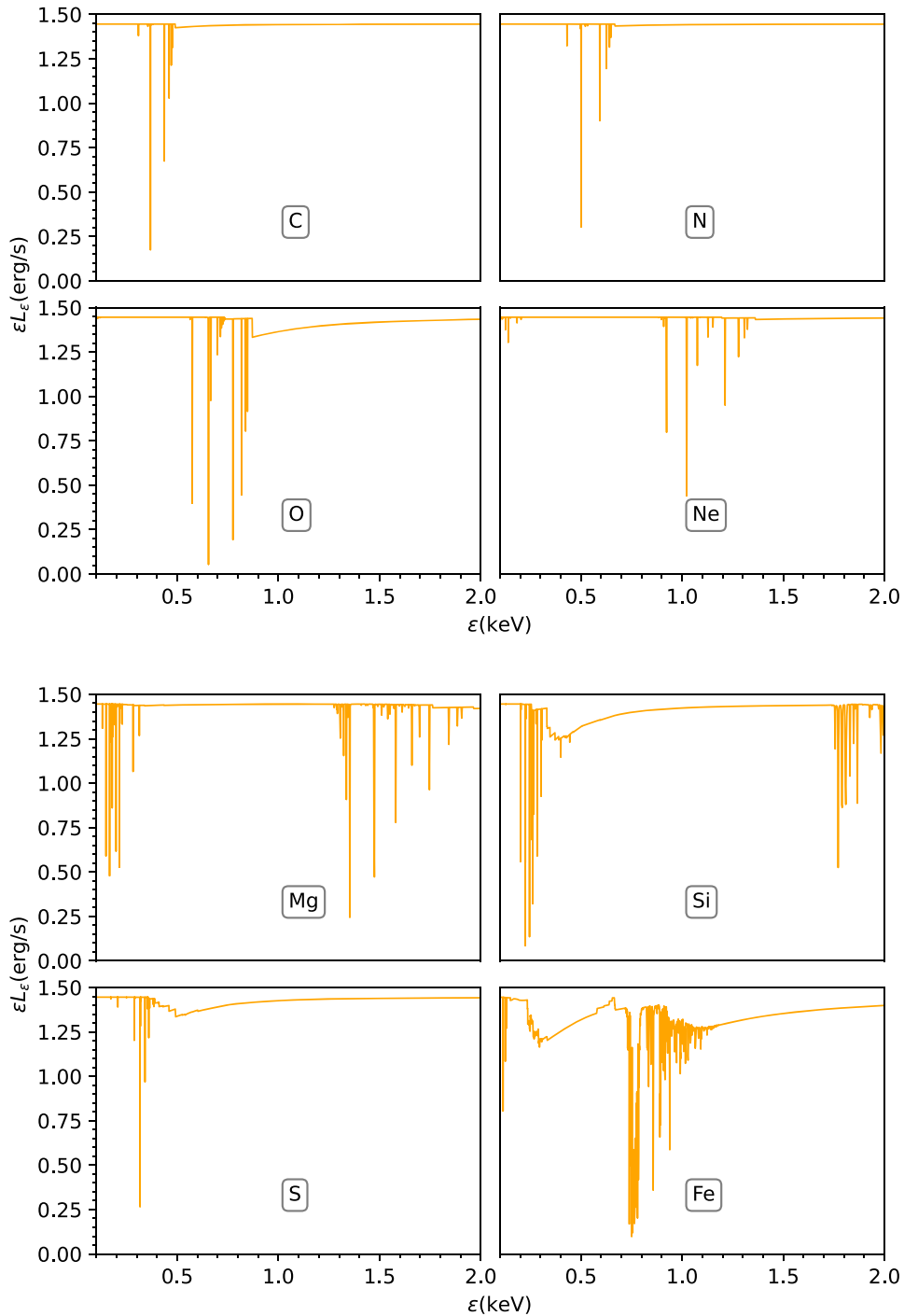


Figure 7. The elemental contribution in the absorption spectrum. The y-axes represent the transmitted luminosities (ϵL_ϵ), and the x-axes represent the photon energies (ϵ). The units of ϵL_ϵ are $10^{43} \text{ erg s}^{-1}$. Each panel contains the low flux equilibrium spectrum caused by different elements. It is seen that O, Si, S, and Fe contribute most to the absorption spectra.

continues to exhibit absorption features. The time corresponding to this particular state is $\sim 4.6 \times 10^4$ s.

Finally, the fourth panel represents the point at which the source's luminosity begins to decrease, which corresponds to the fourth vertical dashed line from the left in the light curve in Figure 4.

The remaining four panels in Figure 8 depict the time evolution of the emergent spectra after the flare has completely emerged from the cloud. These spectra are compared to the instantaneous equilibrium spectra. In these panels, even after

the flare has passed, the time-dependent spectra continue to evolve, gradually approaching a low-luminosity equilibrium absorption spectrum. The ongoing evolution is particularly noticeable in the edges and some lines in the spectra. The absorption lines below 0.25 keV, around 1.3 keV, and at approximately 1.8 keV exhibit clear changes and evolution over time. The first absorption edge shows an apparent evolution pattern. This is because of the effect of longer equilibrium timescale of ions such as Si XIII, Si XIV, Fe XV, and Fe XVI as shown in Figure 6. As the gas within the cloud settles

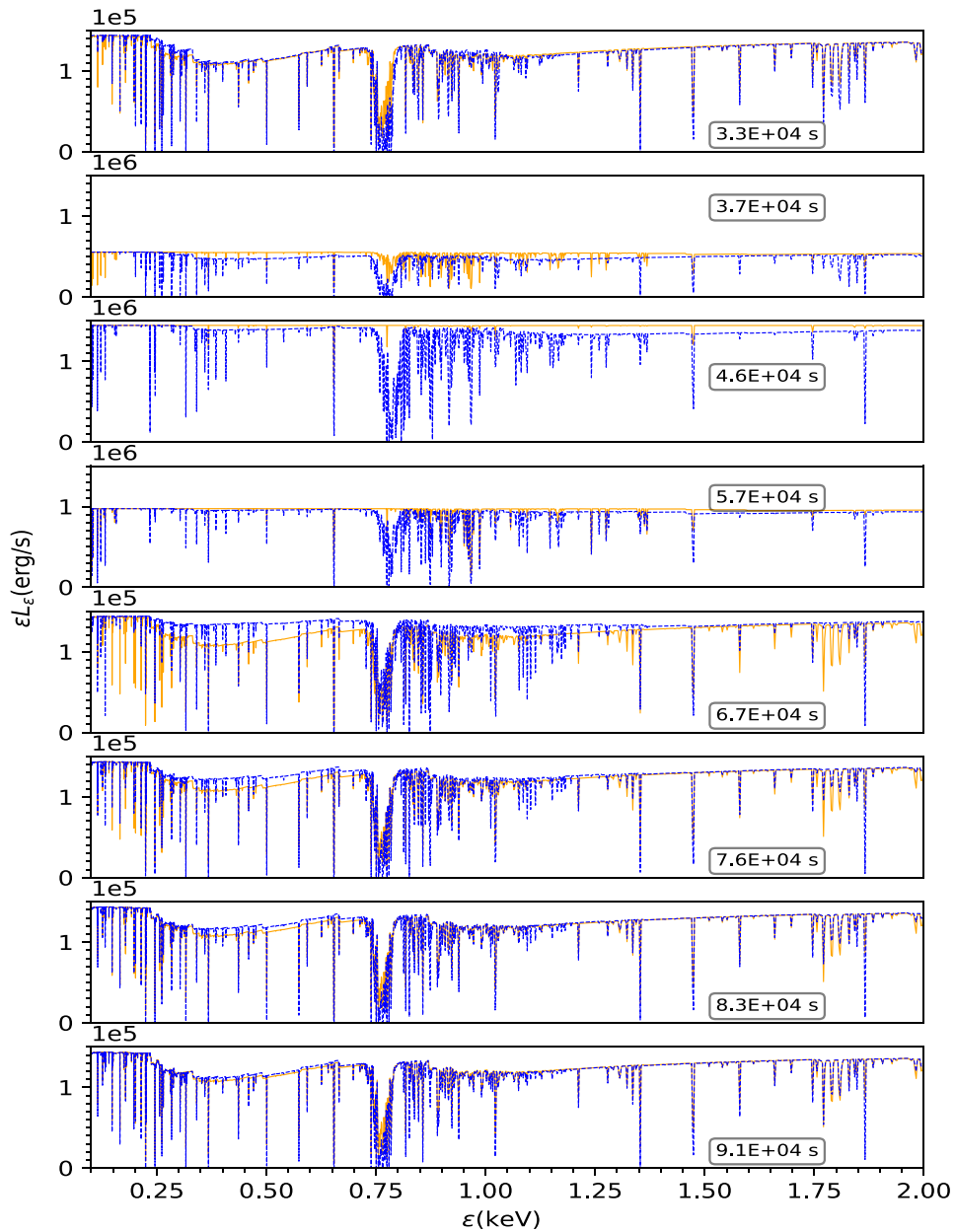


Figure 8. The evolution of the absorption spectra (blue curves) compared against the instantaneous flux equilibrium spectra (orange curves) for model 2. The y-axes represent the transmitted specific luminosities (ϵL_ϵ), and the x-axes represent the photon energies (ϵ). The units of ϵL_ϵ are 10^{38} erg s^{-1} . Each panel corresponds to time as indicated by green vertical dashed and dotted lines in the light curve in Figure 4. Note that the range of the y-axis is not the same for all panels. This is because the ionizing continuum of the source for this model changes by a factor of 10. The multiplicative factors for y-axes are shown at the upper left corner of each panel.

into a low-luminosity ionization equilibrium state, these lines continue to shift and evolve. The evolving nature of the spectra is indicative of the ongoing processes and adjustments occurring within the gas cloud. It highlights the time it takes for the ionization and excitation states of the gas to reach a stable equilibrium configuration after the passage of the flare.

According to the model, the cloud takes $\sim 9.1 \times 10^4$ s to reach this low-luminosity ionization equilibrium state. During this period, the time-dependent spectra gradually converge toward the equilibrium absorption spectrum. By studying the time evolution of the emergent spectra in these panels, one can gain insights into the relaxation and settling processes of the gas cloud following the flare event. The changes in the absorption features, particularly in the edges and lines, provide

valuable information about the ionization and the timescales involved in reaching a stable equilibrium state.

The absorption features change rapidly during the evolution. This is primarily due to the ionization of Fe from M-shell ions such as Fe XV, Fe XVI, and Fe XVII, whose simple atomic structure does not have the rich inner shell spectra of the M-shell ions but contributes most to the absorption. It is also worth pointing out that the effects of saturation can be to make absorption features vary less with time than the abundances of their ions. Thus, strong lines appear to be less variable than the ions. Turbulent broadening plays a role in determining the importance of saturation. In AGN outflows, typical turbulent velocities are $\sim 10^3$ km s^{-1} , which will reduce the optical depths for many resonance lines. These effects are included in our simulation.

5. Results: Model 3, Flare Model with Single-zone Approximation

The alternative approach of modeling WA spectra using a single-zone approximation offers a computationally cheaper alternative to including radiative transfer in the calculations. In this method, the entire cloud is treated as a single zone, neglecting spatial variations and radiative transfer effects.

The modeling begins by calculating the time-dependent level population at the face of the cloud, solving the ion fraction, and heating and cooling equations for variable incoming radiation. It is then assumed that the evolution of the ion fraction pattern is the same throughout the cloud. This simplified approach produces spectra, as shown in Figure 9, which we refer to as model 3.

However, it is important to note that the timescale of evolution differs in the single-zone approximation compared to the multiple-zone approach. By neglecting radiative transfer effects, important phenomena such as the absorption of ionizing radiation and geometric dilution are excluded. Consequently, the evolution of the ion fractions inside the cloud differs from that at the face of the cloud. Nevertheless, for thin gas clouds, the single-zone approximation may provide sufficiently accurate results. In this section, we examine this possibility.

Examining Figure 9, the top panel represents the initial state when the ionizing flux is at a low level, corresponding to the case before the light reaches the back of the cloud. As the increased flux passes through the entire cloud, the time-dependent spectra start to diverge from the equilibrium spectra associated with the instantaneous flux equilibrium spectra. This divergence is observed in the second, third, fourth, fifth, and sixth panels. Eventually, the time-dependent spectrum nearly overlaps with the equilibrium spectrum in the last panel, indicating that the ion fraction has reached the equilibrium value by that time.

In the single-zone approximation, the absence of radiative transfer calculations leads to the exclusion of the time delay caused by absorption. Consequently, this method predicts the simultaneous change in optical depth at the face of the cloud and inside the cloud. This is unlikely to happen in reality. There is some lag in the evolution of the ion at different points in the cloud owing to the fact that the radiation needs to bleach through the cloud. This effect is particularly evident in the absorption spectrum and becomes more pronounced with a greater physical thickness of the gas. In the present model, the spectrum does not converge well to the final low flux equilibrium spectrum, as observed in the multiple-zone model. This is more visible at the first absorption feature. The absorption lines at ~ 1.8 keV also did not quite overlap with the absorption lines that come from equilibrium approximation, which is given in orange. This discrepancy arises from the different ion fractions and their evolution at the front and back of the absorber, as depicted in Figure 6. Specifically, ions such as Si XIII, Si XIV, Fe XV, and Fe XVI exhibit different ion fraction values at the front and back of the cloud during specific stages of evolution.

The discrepancy between single-zone and multiple-zone approach modeling is illustrated by Figure 10. This figure shows the ratio of the emergent specific luminosity for single-zone to multiple-zone approximations. The ratio is expected to be 1 if both techniques produce the same results. However, the figure shows that the ratio is greater than 1 for some specific

wavelengths where the absorption lines appear in the spectrum. This means that the depths of the absorption lines in the single-zone model are underestimated compared with the multiple-zone model. In the case of the multiple zones, the cloud is divided into many spatial zones, and the absorption by each zone is calculated to find a radiation field throughout the cloud, which is used to find the ionization state. This process incorporates absorption and geometric dilution, resulting in different ion fractions from the single-zone approximation deeper in the cloud. The effect is significant for those energy values where opacity is high, and this is why the two methods diverge more in the lines than in the continuum. The spikes in Figure 10 correspond to the ratio of absorption lines. The ratio is highest at 0.75 keV. This energy corresponds to the absorption lines from L-shell iron ions.

In summary, the single-zone approximation offers a computationally efficient approach for modeling WA spectra. While it neglects radiative transfer effects and the associated time delays, it can still provide valuable insights, particularly for thin gas clouds. The differences observed in the ion fraction evolution and absorption spectra between the front and back of the cloud emphasize the limitations of this approach compared to more detailed multiple-zone models.

6. Conclusion

Understanding WAs is essential for gaining insights into AGNs and their surrounding environments (Reynolds et al. 1995; Blustin et al. 2005; Sanfrutos et al. 2018; Kallman & Dorodnitsyn 2019). When the illuminating flux undergoes variations comparable to the ionization, recombination, and propagation timescales in WA clouds, relying solely on photoionization and thermal equilibrium assumptions can yield misleading interpretations when analyzing observations. This study addresses these challenges by incorporating AGN source variability and employing nonequilibrium photoionization calculations to model the outflow. The main focus of this research is on the high-resolution spectrum and its temporal evolution, a crucial aspect for forthcoming missions like XRISM and Athena. The developed model is particularly suited for analyzing the soft X-ray band (0.1–2 keV). By fitting the evolving spectrum to a variable ionizing continuum, valuable information about the WA's properties, such as density, location, and ionization state, can be extracted and constrained. This paper introduces the concept of employing time-dependent photoionization calculations to accurately track changes in the absorber's ionization state over time. For the specific light curve considered in this study (model 1), the equilibration time for the spectral response is estimated to be $\sim 5.8 \times 10^6$ s.

In this study, we have incorporated two fundamental types of variability, namely step-up and flare, which closely resemble real-world scenarios. Sudden increases in source luminosity due to accretion rise are common in AGNs (McHardy et al. 2004; Uttley & McHardy 2005; Ponti et al. 2012; Vagnetti et al. 2016), and we have extensively examined and presented the properties of the WA during flare events. The micro-physical timescales play a significant role in responding to the variation of the ionizing continuum and depend on factors such as density. At higher densities the gas tends to remain closer to equilibrium, while at lower densities the gas is less responsive to changes in illumination. For intermediate densities, simulations like the ones presented in this study are crucial. By

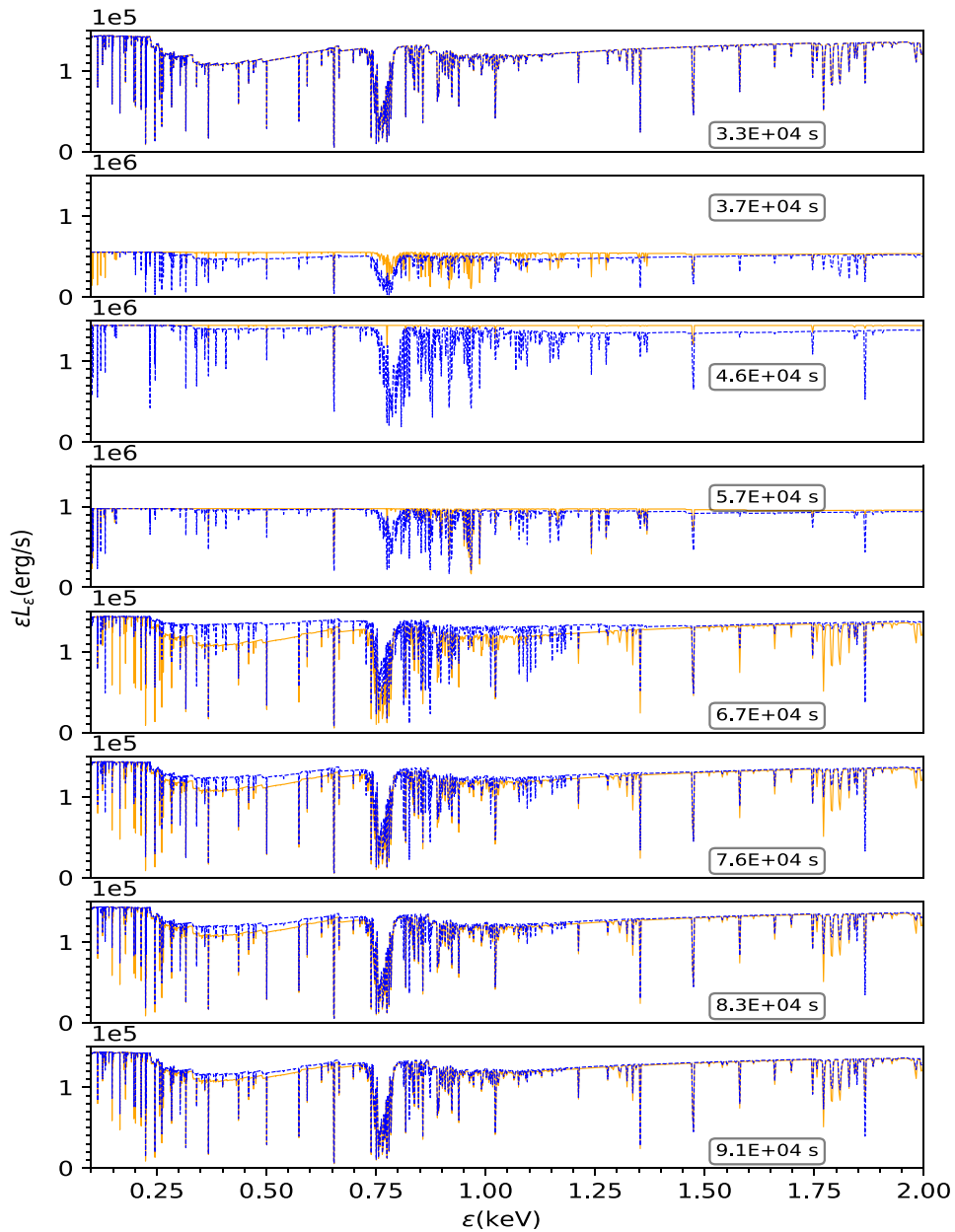


Figure 9. The evolution of the absorption spectra (blue curves) compared against the instantaneous flux equilibrium spectra (orange curves) for model 3. The y-axes represent the transmitted luminosities (ϵL_ϵ), and the x-axes represent the photon energies (ϵ). The units of ϵL_ϵ are 10^{38} erg s^{-1} . Each panel corresponds to the time indicated by green vertical dashed and dotted lines in the light curve in Figure 4. Note that the range of the y-axis is not the same for all panels. This is because the ionizing continuum of the source for this model changes by a factor of 10. The multiplicative factor for y-axis is written at the upper left corner of each panel.

carefully tracking the ionization state and absorption spectra, we can deduce vital information, particularly the density, about the WAs. This knowledge contributes to our understanding of AGN morphology, AGN dynamics, and the role of WAs in AGN feedback. This research lays the foundation for further advancements in this field. For the flare model (model 2), we observed that it takes approximately 9.1×10^4 s for the spectrum to settle down to a state of low flux equilibrium.

WA spectra are commonly studied and analyzed by fitting multiple equilibrium components, with each component parameterized by a single ionization parameter (Reynolds 1997; Blustin et al. 2002; Kaastra et al. 2002; Behar et al. 2003; Laha et al. 2014). Past time-dependent photoionization studies of WAs have overlooked a crucial element: the effect of time-dependent radiative transfer, that is, the coupling of the time-dependent

ionization of the gas, and hence its opacity, with the transport of the radiation. In our work, we have taken coupled time-dependent photoionization and radiative transfer into account by solving the time-dependent transfer equation through multiple spatial zones of ionized gas. Although computationally demanding, this approach is more representative of the actual behavior within the WA. Our study demonstrates that the choice between single- and multiple-zone models has a significant impact on the spectral evolution of the specific model considered here. The disparity becomes even more pronounced with higher column density. A comparison of models with and without time-dependent radiative transfer shows that they undergo distinct spectral evolutions, highlighting differences in timescales and patterns. By accounting for the propagation of the flare through the cloud and incorporating the associated propagation time, the multiple-zone model provides a

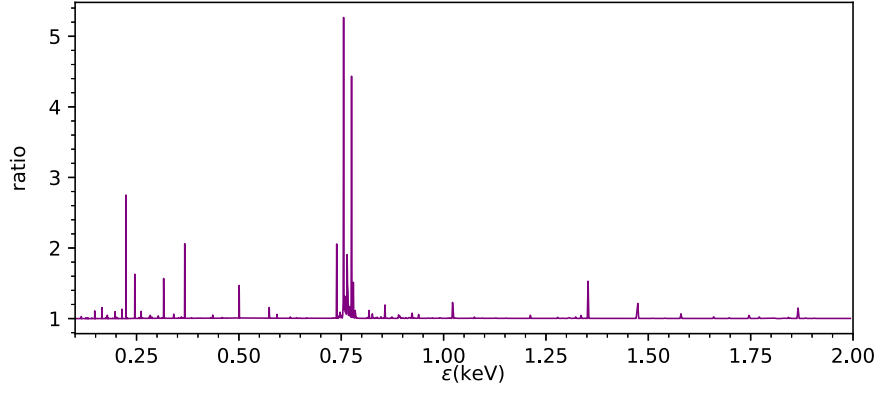


Figure 10. The ratio of emergent specific luminosity for model 3 (single zone) to model 2 (multiple zones) at a time 9.1×10^4 s, which are the last panels of Figures 8 and 9. This demonstrates the difference between the two modeling approaches, and model 3 underpredicts the strengths of absorption features systematically.

more realistic representation of the temporal evolution and smoothing of the flare as it interacts with the gas cloud.

Acknowledgments

We thank Dr. Alan Hindmarsh from Lawrence Livermore National Laboratory for his help and valuable suggestions regarding the ordinary differential equation solver package. We are grateful to the anonymous referee for the constructive feedback. This work was partly funded via NASA grant 17-ATP17-0113 through the Astrophysics Theory Program.

Appendix A Theory

Our models consist of the solution of the coupled equations describing level populations, temperature, and radiation field. Paper I presents all these equations' details. Here we briefly repeat some of them.

A.1. Level Populations

The population of an atomic level obeys the kinetic equation involving the atomic rates into and out of the level,

$$\frac{dn_{i,X}}{dt} = \sum_{j=1}^p n_{j,X} R_{ji} - \sum_{k=1}^p n_{i,X} R_{ik}, \quad (\text{A1})$$

and the equation of number conservation,

$$\sum_{i=1}^p n_{i,X} = xn_{\text{H}}, \quad (\text{A2})$$

where $n_{i,X}$ are the level populations in i th energy level of element X in units of cm^{-3} , which is equal to the product of the fractional elemental abundance and total hydrogen number gas density, n_{H} . Parameter x is the fractional elemental abundance of species X relative to hydrogen. R_{ji} is the transition rate from the j th to i th energy level contributed by atomic processes, including photoexcitation, photoionization, collisional excitation, collisional ionization, recombination, charge transfer, and radiative decay. The values of rates for R_{ij} are taken from XSTAR. Parameter p is the total number of energy levels considered for the particular element. As discussed in Section 3, we adopt a simplified level structure so that, for an element with atomic number Z , $p = 2Z + 1$. Here and in what follows, we adopt the values of the atomic constants (e.g.,

photoionization cross sections, atomic energy levels, collision rate coefficients) from the XSTAR database (Bautista & Kallman 2001).

A.2. Temperature

The temperature variation in the gas is given by the following differential equation:

$$\frac{dT}{dt} = \frac{2}{3kn_t} \left(\Gamma^{\text{heat}} - \Lambda^{\text{cool}} - \frac{3}{2}kT \frac{dn_t}{dt} \right), \quad (\text{A3})$$

where T is the temperature, Γ^{heat} and Λ^{cool} are total heating and cooling rates in units of $\text{erg s}^{-1} \text{cm}^{-3}$, k is the Boltzmann constant, and n_t is the total number density of particles, i.e., the sum of all electrons, ions, and neutral atoms. The last term on the right-hand side of this equation is the rate of change in the internal energy density associated with the rate of change of the total number of free particles in the gas. This is negligible when the gas is highly ionized; otherwise, it explicitly couples the level populations with the temperature equation.

A.3. Time-dependent Radiative Transfer

The equation describing the time evolution of the radiation field in spherical symmetry is (Hatchett et al. 1976; García et al. 2013)

$$\frac{1}{c} \frac{\partial L_{\epsilon}(R, t)}{\partial t} + \frac{\partial L_{\epsilon}(R, t)}{\partial R} = 4\pi R^2 j_{\epsilon} - \kappa_{\epsilon}(R, t) L_{\epsilon}(R, t), \quad (\text{A4})$$

where R is the distance in the cloud from the ionizing source, $L_{\epsilon}(R, t)$ is the specific luminosity of the ionizing source in $\text{erg s}^{-1} \text{erg}^{-1}$, j_{ϵ} is the local emissivity in $\text{erg s}^{-1} \text{cm}^{-3} \text{erg}^{-1}$, and $\kappa_{\epsilon}(R, t)$ is the total extinction coefficient in cm^{-1} . In our calculations in this paper, the extinction comes from only absorption and we do not include emission, so the equation becomes

$$\frac{1}{c} \frac{\partial L_{\epsilon}(R, t)}{\partial t} + \frac{\partial L_{\epsilon}(R, t)}{\partial R} = -\kappa_{\epsilon}(R, t) L_{\epsilon}(R, t). \quad (\text{A5})$$

The rest of the equations for different timescales and their comparison are mentioned in detail in our previous work (Paper I). We have generated a mini version of the full XSTAR database, including only three levels; one ground, one excited, and one ionized level. This newly generated database is then tested with multiple methods and verified to produce adequate accuracy in our time-dependent computation. The readers are

encouraged to review our previous paper (Paper I). The recombination, photoionization, and light-travel time play an important role in the evolution and equilibration of the gas when it experiences variable ionizing radiation. The recombination time is the most important out of them, which essentially depends on the density of the gas.

Appendix B Numerical Approach

The set of ordinary differential equations for our problem governs level populations, temperature, electron number density, and radiation field. In the general case, this system of equations can have terms that cover a large range of values, due to the diverse physical processes they describe. This system is, therefore, “stiff” (Cooper 1969), that is, they correspond to a set of variables (solutions of differential equations) changing from a much faster rate to a much slower rate. Some processes are important for small timescales, while others dominate for long timescales. In order to solve these equations, we implement the well-known ordinary differential equation solver, DVODE (Brown et al. 1989).

ORCID iDs

Dev R. Sadaula  <https://orcid.org/0000-0002-9163-8653>
Timothy R. Kallman  <https://orcid.org/0000-0002-5779-6906>

References

Bautista, M. A., & Kallman, T. R. 2001, *ApJS*, 134, 139
Behar, E., Rasmussen, A. P., Blustin, A. J., et al. 2003, *ApJ*, 598, 232

Blustin, A. J., Branduardi-Raymont, G., Behar, E., et al. 2002, *A&A*, 392, 453
Blustin, A. J., Page, M. J., Fuerst, S. V., Branduardi-Raymont, G., & Ashton, C. E. 2005, *A&A*, 431, 111
Brown, P. N., Byrne, G. D., & Hindmarsh, A. C. 1989, *SIAM J. Sci. Stat. Comput.*, 10, 1038
Cooper, G. 1969, *FEBS Lett.*, 2, S22
García, J., Elhoussieny, E. E., Bautista, M. A., & Kallman, T. R. 2013, *ApJ*, 775, 8
Gnat, O. 2017, *ApJS*, 228, 11
Hatchett, S., Buff, J., & McCray, R. 1976, *ApJ*, 206, 847
Kaastra, J. S., Steenbrugge, K. C., Raassen, A. J. J., et al. 2002, *A&A*, 386, 427
Kallman, T., & Bautista, M. 2001, *ApJS*, 133, 221
Kallman, T., & Dorodnitsyn, A. 2019, *ApJ*, 884, 111
Kallman, T. R., & McCray, R. 1982, *ApJS*, 50, 263
Kaspi, S., Brandt, W. N., Netzer, H., et al. 2001, *ApJ*, 554, 216
Laha, S., Guainazzi, M., Dewangan, G. C., Chakravorty, S., & Kembhavi, A. K. 2014, *MNRAS*, 441, 2613
Luminari, A., Nicastro, F., Krongold, Y., Piro, L., & Thakur, A. L. 2023, *A&A*, 679, A141
McHardy, I. M., Papadakis, I. E., Uttley, P., Page, M. J., & Mason, K. O. 2004, *MNRAS*, 348, 783
Nicastro, F., Fiore, F., Perola, G., & Elvis, M. 1999, *ApJ*, 512, 184
Ponti, G., Papadakis, I., Bianchi, S., et al. 2012, *A&A*, 542, A83
Proga, D., Waters, T., Dyda, S., & Zhu, Z. 2022, *ApJL*, 935, L37
Reynolds, C. S. 1997, *MNRAS*, 286, 513
Reynolds, C. S., Fabian, A. C., Nandra, K., et al. 1995, *MNRAS*, 277, 901
Rogantini, D., Mehdipour, M., Kaastra, J., et al. 2022, *ApJ*, 940, 122
Sadaula, D. R., Bautista, M. A., García, J. A., & Kallman, T. R. 2023, *ApJ*, 946, 93
Sanfrutos, M., Longinotti, A. L., Krongold, Y., Guainazzi, M., & Panessa, F. 2018, *ApJ*, 868, 111
Silva, C. V., Uttley, P., & Costantini, E. 2016, *A&A*, 596, A79
Tarter, C. B., Tucker, W. H., & Salpeter, E. E. 1969, *ApJ*, 156, 943
van Adelsberg, M., & Perna, R. 2012, *MNRAS*, 429, 1407
Uttley, P., & McHardy, I. M. 2005, *MNRAS*, 363, 586
Vagnetti, F., Middei, R., Antonucci, M., Paolillo, M., & Serafinelli, R. 2016, *A&A*, 593, A55